

Compression, Impact and Hot Rebound Flows from Coronal Rain Downflows

J. Wachira,¹ P. Antolin,¹ 

¹School of Engineering, Physics and Mathematics, Northumbria University, Newcastle upon Tyne, NE1 8ST, UK

Accepted XXX. Received YYY; in original form ZZZ

arXiv:2509.11627v1 [astro-ph.SR] 15 Sep 2025

ABSTRACT

Understanding the processes associated with coronal rain due to the thermal non-equilibrium (TNE) and thermal instability (TI) scenario can help us understand coronal heating. We aim to study the properties of a quiescent coronal rain event and its effect on the solar atmosphere. We utilise space-based data from the *High-Resolution Imager in Extreme Ultraviolet* of Solar Orbiter, the *Atmospheric Imaging Assembly* of the Solar Dynamics Observatory, and the Slit-Jaw Imager (SJI) from the *Interface Region Imaging Spectrograph* from November 1st, 2023. During the coronal rain shower, the coronal loop exhibits large EUV variability and drastic changes in sub-structure. Coronal rain clumps with total velocities between 72 km s^{-1} and 87 km s^{-1} and cool EUV absorbing core sizes of $\approx 600 \text{ km}$ and densities of $\approx 5 \times 10^{11} \text{ cm}^{-3}$ are seen to fall with a strong compression ahead. During the compression we measure a low polytropic index with $\gamma = 1.085$, suggesting the presence of molecules. The rain shower carries a total of $3.09 \times 10^{26} \text{ erg}$, and the clumps produce impacts seen in all EUV channels and in SJI 1400 Å. The impacts generate hot rebound flows with temperatures of $10^{6.2} - 10^{6.3} \text{ K}$ and velocities of $85 - 87 \text{ km s}^{-1}$, which refill and reheat the loop but carry less than 20% of the clumps' kinetic energies. We find signatures of a steady footpoint heating, in agreement with the TNE-TI scenario, with an estimated amplitude of $2.56 \times 10^{-2} \text{ erg cm}^{-3} \text{ s}^{-1}$ in agreement with active region estimates. Coronal rain may therefore be a good proxy for the total integrated heating that gives birth to TNE-TI.

Key words: Sun: transition region – Sun: corona – Sun: activity – Sun: filaments, prominences – Magnetohydrodynamics – Instabilities

1 INTRODUCTION

Until the 1940s, it was widely accepted that temperatures within the sun decrease radially outwards. However, this viewpoint was called into question and a discovery (Grotrian 1934; Edlen 1945) was made indicating that the solar corona reheats to temperatures exceeding millions of degrees Kelvin. The heating mechanism behind coronal heating has eluded scientists for many years to what is now known as the ‘coronal heating problem’. Through the help of countless observations and numerical simulations (Van Doorn et al. 2020; van der Holst et al. 2014; Dere 1994) it is evident that the heating mechanism involves the release of magnetic energy through processes such as magnetic reconnection and magnetohydrodynamic (MHD) waves.

Coronal loops consist of magnetic field lines shaped like loops that are anchored to the solar surface and contain ionised plasma. The plasma is frozen-in to the magnetic field lines due to the high magnetic Reynolds number. There are many mysteries to coronal loops, namely, their lifespan and morphology. Observations (Reale 2014) have identified filamentary substructures within coronal loops, leading to the concept known as coronal strands (Klimchuk 2015). The widths of these coronal strands have been measured to be a few hundred kilometres (Williams et al. 2020; Peter et al. 2013; Brooks et al. 2013; Aschwanden & Boerner 2011). Not all coronal loops

show coronal strands, and it has been proposed that strands appear during the coronal loops cooling phase, and particularly the formation of coronal rain, due to the condensation-corona transition region (CCTR), as observed by Antolin et al. (2023) in high-resolution with EUI_{HRI/EUV} of Solar Orbiter (SolO) (Müller et al. 2020; Rochus et al. 2020), which is also supported by numerical simulations (Antolin et al. 2022).

Some of the first reports of coronal rain date from the 1970s by Kawaguchi (1970); Leroy (1972) but it gained significant recognition only in the last decade. Coronal rain is characterised as cool, dense and clumpy plasma that exhibits temperature ranges from $10^3 - 10^5 \text{ K}$ and number density ranges of $10^{10} - 10^{13} \text{ cm}^{-3}$. Coronal rain appears over the order of minutes and is most easily seen when observed off the limb, when it is seen in emission in chromospheric lines such as H α and Ca II H or in transition region lines such as Si IV 1402 Å. Studies by Antolin & Rouppe van der Voort (2012) have observed coronal rain to have a broad velocity distribution of $10 - 150 \text{ km s}^{-1}$, peaking between $50 - 100 \text{ km s}^{-1}$. The widths vary depending on the spatial resolution and the opacity of the spectral line of observation, averaging around $200 - 500 \text{ km}$ in the optical spectrum and $500 - 600 \text{ km}$ in the UV and EUV (Antolin et al. 2015; Antolin et al. 2023). Other studies, such as Şahin et al. (2023), have found widths twice higher in the UV and EUV probably due to the lower spatial resolution. The references stated above show that rain lengths also exhibit a dependence but at a minor degree on the wavelength of observation, and are more sparsely distributed than the

* E-mail: patrick.antolin@northumbria.ac.uk

widths. Lengths in the optical spectra peak around 700 – 1000 km, but about twice this value in the UV and low-temperature EUV lines. However, a long distribution tail is observed to higher length values for all wavelengths. For a review of the coronal rain properties please see [Antolin & Froment \(2022\)](#).

In addition to the descending coronal rain, the recent study by [Antolin et al. \(2023\)](#) identified an atmospheric response to the rain impact. They found speeds of the upward propagating features following the rain impact in the range of 50 – 130 km s⁻¹, and interpreted the lower and upper values in this range as corresponding to upflows and rebound shocks, respectively. This atmospheric response associated with coronal rain has also been predicted in numerical studies, e.g. by [Müller et al. \(2003\)](#).

Neighboring coronal rain clumps are commonly observed to fall in tandem with each other, spanning over a wide cross-section of coronal loops. This phenomenon is known as a ‘rain shower’ ([Antolin & Rouppe van der Voort 2012; Şahin & Antolin 2022](#)). Local thermal instability (TI) within a coronal loop in a state of thermal-non-equilibrium (TNE) is said to be the cause of coronal rain, and is also thought to be the synchronising mechanism leading to rain showers. This is supported by numerical simulations by [Fang et al. \(2013\)](#), where a first TI-driven condensation perturbs neighboring critically stable field lines leading to a fast growth of the condensation in the direction perpendicular to the field. TNE occurs when there is strongly stratified and relatively long lasting heating. Namely, the loop footpoints need to be heated roughly ten times more than the loop apex, without much heating asymmetry between the two footpoints and the heating needs to be sustained longer than the radiative cooling time ([Klimchuk & Luna 2019; Johnston et al. 2019](#)). After a rapid heating phase, the coronal loop becomes increasingly dense due to sustained chromospheric evaporation, which in turn leads to an over-density compared to that needed to achieve thermal equilibrium. Radiative losses then become larger than the input from thermal conduction and enthalpy, leading to a runaway cooling and localised TI in the corona. Condensations occur, which fall as coronal rain largely evacuating the loops. This TNE-TI scenario repeats if the heating persists, leading to TNE-TI cycles of heating and cooling that manifest as long-period EUV intensity pulsations ([Auchère et al. 2014; Froment et al. 2015](#)) and periodic coronal rain ([Auchère et al. 2018](#)).

However, there is still an ongoing debate on the role of TI, and the exact route to catastrophic cooling ([Klimchuk 2019; Waters & Stricklan 2024](#)). Furthermore, the overall prevalence of TNE-TI in the solar atmosphere is unknown. [Şahin et al. \(2023\)](#), conducted a statistical analysis of the ‘rain showers’ for one active region (AR) and found the coronal volume in a state of TNE-TI to be at least 50% the AR volume. Determining the coronal volume subject to TNE-TI is important because of its strong link to coronal heating. Indeed, the specific spatiotemporal distribution of heating required to produce coronal rain constitutes a strong constraint for heating mechanisms.

[Antolin et al. \(2022\)](#) conducted 2.5D radiative MHD simulations which depict TI-driven catastrophic cooling leads to the formation of cool and dense cores at the head of the rain emitting in chromospheric lines. These cores are surrounded by thin but strongly emitting shells in TR lines that elongate in the wake of the rain, in what is known as the condensation corona transition region (CCTR).

There are three different types of coronal rain ([Antolin & Froment 2022](#)). The first is the quiescent type usually observed in non-flaring ARs and does not rely on a specific magnetic topology. This study focuses on this type. The second is flare-driven coronal rain which is associated with the cool material observed in the gradual phase of flare loops. Lastly, there is a prominence-coronal rain hybrid,

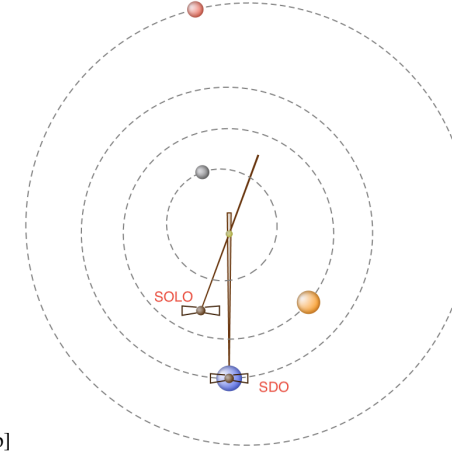


Figure 1. The location of SolO and SDO in relation to the Sun and Earth on November 1st, 2023, obtained from the Propagation Tool software ([Rouillard et al. 2017](#)).

also known as coronal spider or cloud prominence, which involves a complex magnetic field with a fan-spine (null-point) topology at the top of loop arcades.

With the help of the *Atmospheric Imaging Assembly* (AIA, [Lemen et al. 2012](#)) onboard the Solar Dynamics Observatory (SDO, [Pesnell et al. 2012](#)), alongside the Slit Jaw Imager (SJI) onboard the *Interface Region Imaging Spectrograph* (IRIS, [De Pontieu et al. 2014](#)), and the High-Resolution Imager of the Extreme Ultra Violet Instrument (HRI_{EUV}) aboard the Solar Orbiter mission ([Rochus et al. 2020; Müller et al. 2020](#)), this study provides a detailed analysis of quiescent coronal rain observed during the SolO perihelion of November 1st 2023. Through the variety of wavelengths and viewpoints, we examined various properties of coronal rain. In particular, we focus on the compression produced by the rain and its effect on the coronal loop upon impact on the lower atmosphere. In section 2; we discuss our observation; 3; discuss our methodology; 4; discuss our findings; and a detailed analysis is discussed in 5.

2 OBSERVATIONS

We sourced data from the 174 Å passband of the High-Resolution Imager in Extreme Ultraviolet (HRI_{EUV}) instrument aboard Solar Orbiter (SoLO, [Rochus et al. 2020](#)), as well as from the *Atmospheric Imaging Assembly* (AIA, [Lemen et al. 2012](#)) aboard the Solar Dynamics Observatory (SDO) and the Slit-Jaw Imager (SJI) onboard the *Interface Region Imaging Spectrograph* (IRIS, [De Pontieu et al. 2014](#)). To identify the same region between AIA and the HRI_{EUV} data, we utilised the JHelioviewer software developed by [Müller et al. \(2017\)](#).

HRI_{EUV} was positioned at 0.56 AU from the Sun and captured images in a format of 2048 × 2048 pixels. This provided a full field-of-view (FOV) of 1007.6" × 1007.6", with a pixel scale of 0.492 arcseconds per pixel and a pixel sampling of 199.83 km per pixel. The observation began on the 1st of November 2023 at 00:43:41 UT, with the last image recorded at 01:43:31 UT. An extra 3.65 minutes was added to the start and end times to account for the time it takes light to reach the AIA compared to HRI_{EUV}. This observation was part of the ‘R SMALL HRES MCAD AR-Heating’ Solar Orbiter Planning Sheet (SOOP) which provided a cadence of 10 s, an exposure time of 3 s and a total duration of approximately 60 min. In the 174 Å passband, Fe IX (171 Å) and Fe X (174 Å) are the

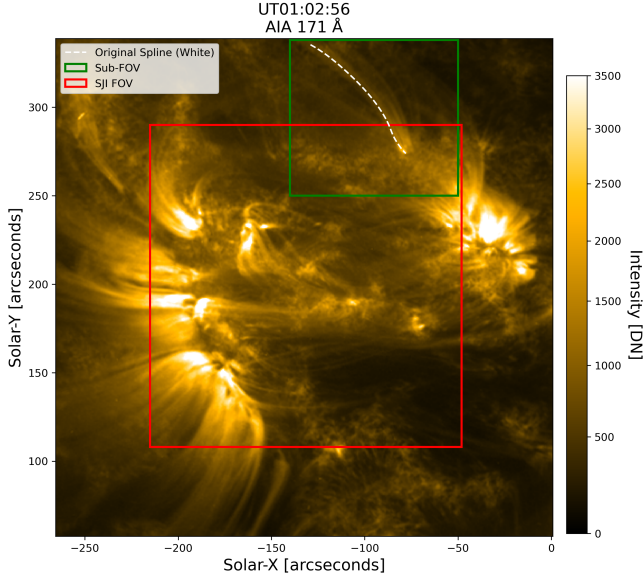


Figure 2. The active region observed in AIA showing the SJI 1400 Å FOV and the sub-FOV shown in Figure 5. The rain trajectory is plotted in white as ‘original spline’

ions that dominate with a peak formation temperature of 10^6 K. The images have been prepped with the `eui_prep` routine to level 2, which reduces jitter and pointing errors. Significant jitter remained and a cross-correlation technique was applied to remove this, following Chitta et al. (2022).

IRIS and AIA level 2 data were obtained from the LMSAL data search website [online], with both instruments positioned at approximately 1 AU from the Sun. We analysed across multiple AIA passbands: 94 Å, 131 Å, 171 Å, 193 Å, 211 Å, 304 Å, 335 Å, 1600 Å and 1700 Å. This broad spectrum allowed for a comprehensive analysis of the impact and effect of the rain on the Sun’s atmosphere.

While most AIA passbands operated at a cadence of 12 s, AIA 1600 Å and AIA 1700 Å operated at a cadence of 24 seconds. AIA has a pixel scale of 0.6 arcseconds per pixel. The AIA dataset obtained for this study starts on the 1st of November at 00:29:26 UT and ends at 01:59:40 UT allowing for a total duration of roughly 90 min. The pixel sampling obtained from AIA is 431 km per pixel.

We use SJI 1400 Å data from IRIS, which predominantly captures the Si iv resonance lines at 1394 Å and 1402 Å, which originate from plasma characteristic of the transition region and have a mean formation temperature of 0.08 MK. The SJI 1400 Å operated with a cadence of 10.5 s and an exposure time of 4 s. Each image obtained by SJI 1400 Å has dimensions of 1001×1093 pixels with a pixel scale of 0.16635 arcseconds per pixel. This provided a full field of view of $166.52'' \times 181.82''$ and a pixel sampling size of 120 km per pixel. The FOV centre is -131.5 WEST and 199.24 North. The observation began on the 1st of November at 00:38:17 UTC and concluded at 01:49:49 UTC allowing for a total duration of approximately 70 min. IRIS conducted a very large sparse 2-step raster observation for this event. The slit did not cross the event and IRIS only partly captured the loop footpoint as shown in Figure 2.

The NOAA 13473 AR seen in Figure 3 exhibited signs of being in its decay phase due to the lack of sunspots and pores as observed from the HMI continuum. Utilising the HMI magnetogram we note that the coronal loop footpoint, where the coronal rain is observed to fall, is anchored into a positive polarity region. The other footpoint

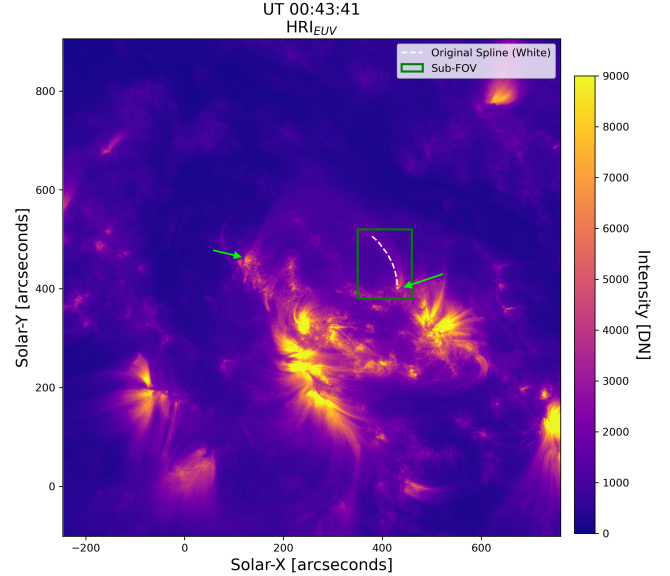


Figure 3. The studied AR on the solar disc with HRI_{EUV}. The sub-FOV enclosed in green is shown in Figure 4. The rain trajectory is plotted in white and is denoted as the ‘original spline’.

anchored into a negative polarity region can also be distinguished. Both footpoints appear to be rooted in moss as depicted by the green arrows in 3.

3 METHODOLOGY

To analyse the coronal rain event, we traced its trajectory with a series of 10 coordinates. Using those 10 coordinates, we generated a cubic spline interpolation, denoted as the ‘original spline’ (in white) in Figures 5 and 4. As a single cubic spline did not capture the entirety of the coronal rain shower, we constructed multiple cubic splines and systematically shifted them along the x -axis relative to the original cubic spline as shown in Figures 4 and 5. The notation $\text{spline} \pm x$ is a shift of the original spline by x pixels in the x -axis, created to capture the extent of the rain shower fully. Furthermore, the width of the rain clump is larger than one cubic spline, hence the need for multiple splines. This methodology was applied consistently in AIA, HRI_{EUV} and SJI 1400 Å.

For AIA, the coronal rain path was first identified in 171 Å with the same cubic spline process previously explained. We then applied these same coordinates across all AIA wavelengths. The cubic splines depicted in Figures 5 and 4 show the only region of the coronal loop where the coronal rain is observed. We then interpolated the intensity values along the cubic splines across all images to create the time-distance diagrams.

To determine the velocity of the descending rain and associated upward propagating features, we select the cubic spline along which the rain signatures are best seen and calculate the slope of the line in the time-distance diagram for that path. Using HRI_{EUV}, the width of the coronal rain clump was assessed by taking a transverse cut across the coronal loop, denoted as path 2 in Figure 4, interpolating the intensity values along the path (path 2 in figure 9) and calculating the Full Width at Half Maximum (FWHM). Additionally, ‘Path 1’ was created to assess the EUV variations across the coronal loop.

We use the Differential Emission Measure (DEM) to estimate

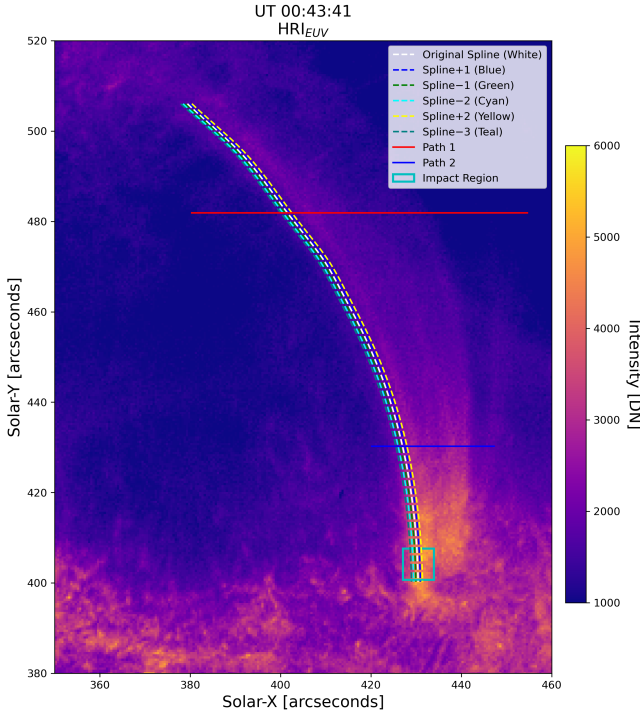


Figure 4. The coronal loop along which the coronal rain is seen to fall with HRI_{EUV}. The ‘Original Spline’ corresponds to the initial coordinates used to trace the rain trajectory. Spline $\pm x$ is a shift of the original spline by x pixels along the x -axis, created to fully capture the extent of the rain shower. ‘Path 1’ is used to assess the EUV variability in the loop, and ‘Path 2’ is used to estimate the FWHM (Figure 9). The ‘Impact Region’ is where the rain is observed to impact the lower atmosphere.

the mean temperature and number density of the hot, optically thin plasma. For a given temperature along the line-of-sight (LOS), the DEM at that temperature is defined as:

$$\text{DEM}(T)dT = \int_0^\infty n_e n_p(T)dl, \quad (1)$$

where n_e and n_p are the electron and proton number densities, respectively, and l denotes the distance along the LOS. The total Emission Measure (EM) is the integration of the DEM over the temperature range:

$$EM = \int_T \text{DEM}(T)dT, \quad (2)$$

and the mean temperature can be estimated through the DEM-weighted temperature:

$$\langle T \rangle_{\text{DEM}} = \frac{\int_T \text{DEM}(T)TdT}{EM}. \quad (3)$$

From equation 1, we can therefore obtain the DEM-weighted electron number density ($\langle n_e \rangle_{\text{DEM}}$):

$$\langle n_e \rangle_{\text{DEM}} = \sqrt{\frac{1.2 \int_T \text{DEM}(T)dT}{l}}. \quad (4)$$

The factor 1.2 comes from the assumption of a highly ionized plasma with 10% helium.

The DEM is calculated in IDL using the CHIANTI (version 10.1

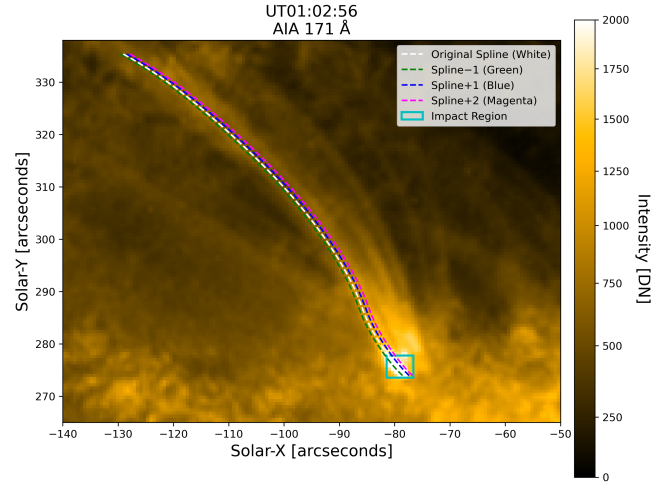


Figure 5. The coronal loop along which the coronal rain is seen to fall in AIA. Same as in Figure 4 but for AIA 171 Å.

developed by Dere et al. (2023) atomic database, first introduced by Dere et al. (1997). The method used is the regularization method discussed in Hannah & Kontar (2012). We selected 16 temperature bins, ranging from $\log_{10} T = 5.5$ to $\log_{10} T = 7.05$ with a bin size of 0.1 in logarithmic space.

4 RESULTS

4.1 Loop Properties

The complementary observations from HRI_{EUV}, AIA and IRIS allow for a thorough analysis from two vantage points of the structure and morphology of the coronal loop affected by the coronal rain event. Although data from IRIS only captures the lower part of the loop, it allows us to pinpoint the loop’s footpoint within the chromosphere and analyse the effects of coronal rain at lower atmospheric layers.

4.1.1 Loop Footpoint

As mentioned in section 2, both footpoints appear to be anchored in moss shown by the green arrows in Figure 3. We observe flash-like EUV brightenings of various sizes at and around the footpoint (see online animation). Multiple small-scale EUV brightenings (only a few pixel wide) appear with typical durations of 50 s, reminiscent of those reported in Berghmans et al. (2021) at the smaller scales. In addition to these, brightenings on the scale of a Mm or more appear as the rain falls, which we describe in detail in section 4.4. Periodic disturbances can also be seen propagating upward along the loop, but only very faintly.

4.1.2 Loop Structure

The estimated total length of the coronal loop observed with HRI_{EUV} is approximately 160 ± 3 Mm. Throughout the observation, notable changes to the loop structure were observed. AIA 171 Å and HRI_{EUV} show the clearest visibility of the loop, suggesting a temperature range of 0.6 to 1 Mk on average. Figures 7 and 8 show the first and last images in AIA 171 Å and HRI_{EUV}, respectively. Initially, the width of the loop taken near the footpoint was 7.2 ± 0.3 Mm and increased

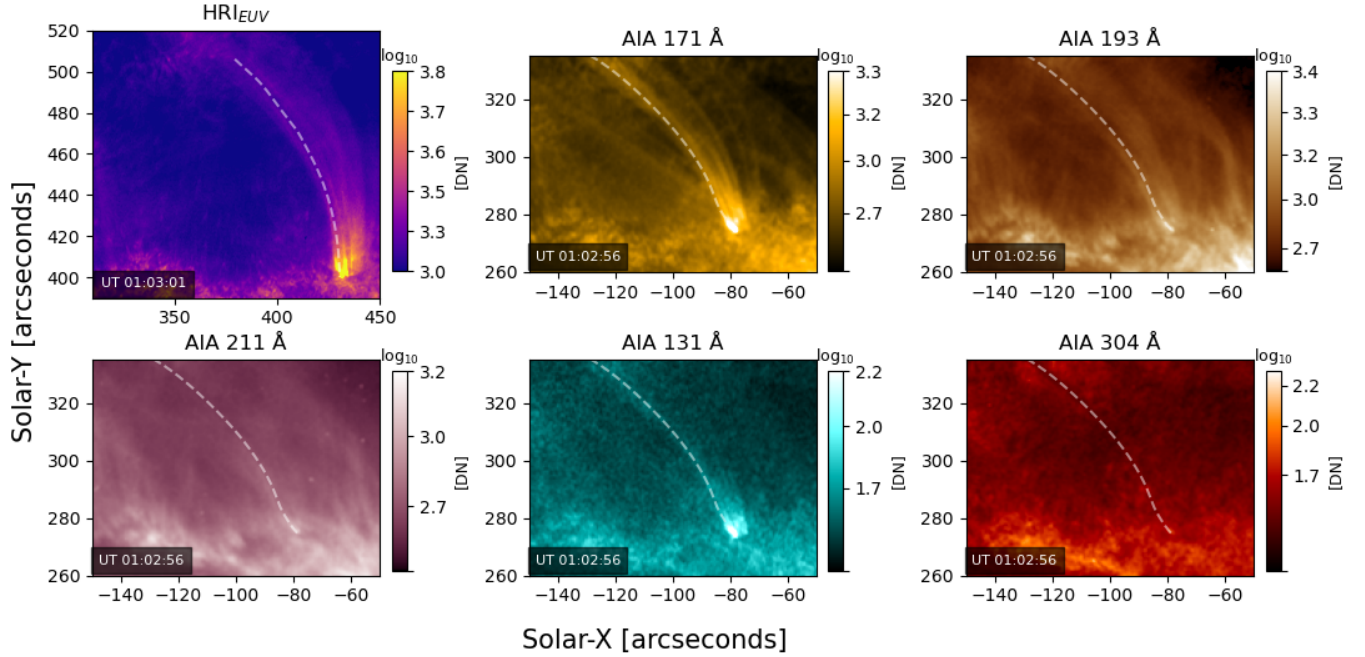


Figure 6. The coronal loop observed in the EUV channels, with the trajectory of the coronal rain clump shown by the white dashed curve at the time of impact of the rain clump with the lower atmosphere. See the online animation.

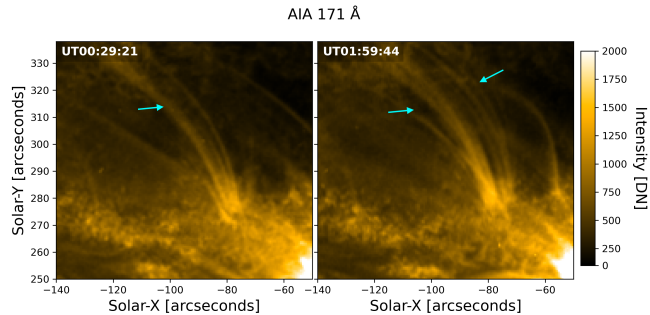


Figure 7. Sub-FOV of AIA 171 Å, for the first (left) and last (right) snapshots of the observation. The cyan arrows point to coronal strands.

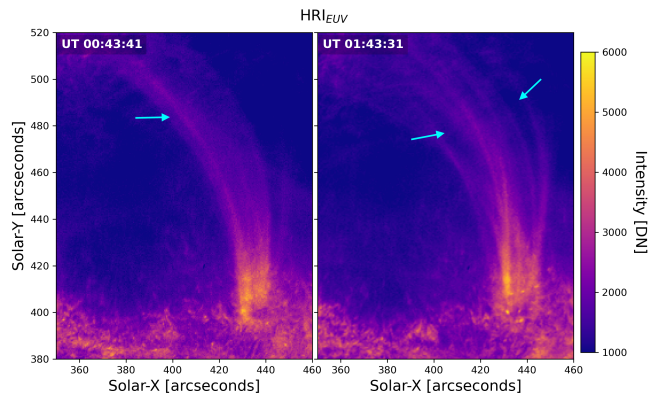


Figure 8. Same as in Figure 7 but for HRI_{EUV}.

to 11.0 ± 0.3 Mm by the end of the observation with HRI_{EUV}. At the beginning of the observation in HRI_{EUV}, the coronal strands are densely packed and exhibit almost uniform intensities, except for one notably brighter strand in the location where the coronal rain is observed to fall. By the end of the observation, new coronal strands appear, while others have disappeared, creating notable gaps between strands. Similar EUV variability with coronal loops is not uncommon and has been discussed in e.g. Ugarte-Urra et al. (2006). Although AIA 171 Å does not show coronal strands as compact as in HRI_{EUV}, potentially due to the different LOS, slightly lower spatial resolution, it does exhibit similar morphological changes between the first and last images.

At the beginning of the observation, AIA 94 Å and 131 Å dominated by Fe xviii (7 MK) and Fe xxI (12 MK) respectively, depict minimal brightening and unclear visibility of the coronal strands. This unclear visibility suggests a lack of high-temperature plasma activity in these wavelength ranges. However, a brightening of a coronal strand, spanning 58 ± 2 Mm in length, on the western end of the loop, occurs approximately 15 – 20 min before the coronal rain impacts, which is likely produced by the lower temperature emission in these passbands.

As the rain falls, compression occurs ahead of the rain. This is composed on one hand of a small-scale brightening, better visible in HRI_{EUV}, immediately ahead of the rain, known as the fireball effect (akin to meteor ablation), which has first been reported in Antolin et al. (2023). On the other hand, a brightening on a larger scale is observed ahead of the rain a few minutes prior to the rain's impact (and culminates with the impact), and is discussed later on. After the impact, a new coronal strand near the loop's centre begins to brighten in HRI_{EUV}.

Figure 9 shows the time-distance diagram along path 1 across the loop in HRI_{EUV} (seen in Figure 4). We can see clear EUV variability in the coronal loop throughout the whole observation. Highlighted

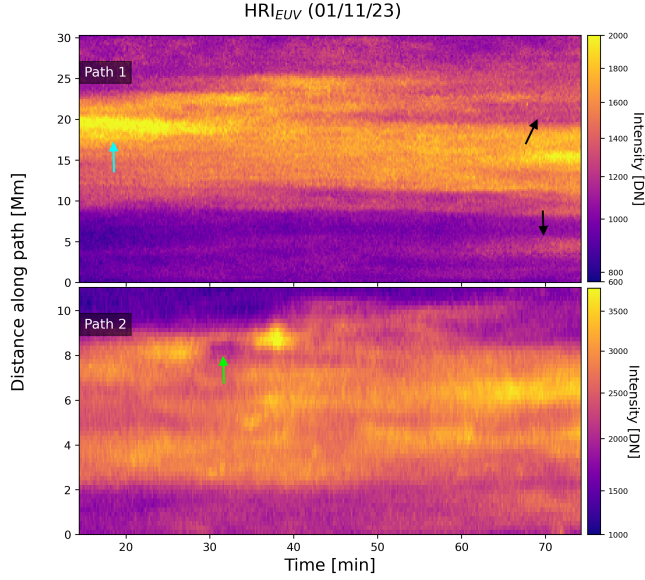


Figure 9. Time-distance diagrams of the two paths shown in Figure 4. The cyan arrow in ‘Path 1’ points to a coronal strand that brightens prior to the rain falling. The black arrows highlight the EUV variability as bright strands appear to fade away and new strands emerge. The green arrow in ‘Path 2’ points to an EUV absorption feature caused by the rain clump.

by the cyan arrow on ‘Path 1’, we see a significant brightening of the same coronal strand where the rain is seen to fall, but at least 15 min prior to the rain passage (see online animation). During this time the strand slowly diminishes in intensity to match the average loop intensity by the time the rain crosses the path. Such brightening, also observed in multiple AIA passbands, is in agreement with thermal non-equilibrium, with parts of the loop catastrophically cooling down as the coronal rain forms. Further down the loop, we took another path denoted as ‘Path 2’ in Figure 9. We see a dim brightening corresponding to the fireball compression, followed by a large absorption feature (highlighted by the green arrow) matching to the time when the rain clump crosses that path, and therefore corresponding to the EUV absorption by the rain’s cool material.

4.2 Rain Properties

4.2.1 Morphology and EUV variability

In Figures 10 and 11 we show the time-distance diagrams created from the cubic splines from Figures 4 and 5, respectively. A downflow corresponding to coronal rain initiates roughly 25 min from the start of the HRI_{EUV} observation and is observed to last for over 15 min in the time interval $t = 27 - 35$ min. The downflow is characterised by a first clear rain clump, which we refer to as ‘downflow 1’ (left cyan arrow in the figures). downflow 1 can be identified in all the cubic splines shown, except the Teal spline (bottom panel in Figure 10), thereby indicating the extent of the rain shower.

To estimate the width of the clump, we use the transverse cut across the loop denoted as ‘Path 2’ in Figure 9, observed with HRI_{EUV}. The aforementioned absorption profile produced by the clump is fitted with a Gaussian, and we use the Full Width at Half Maximum (FWHM) to define the clump’s width. We estimate this width to be 0.55 ± 0.03 Mm. We note that this is not possible with AIA 171 Å since the EUV absorption is not observed in that passband.

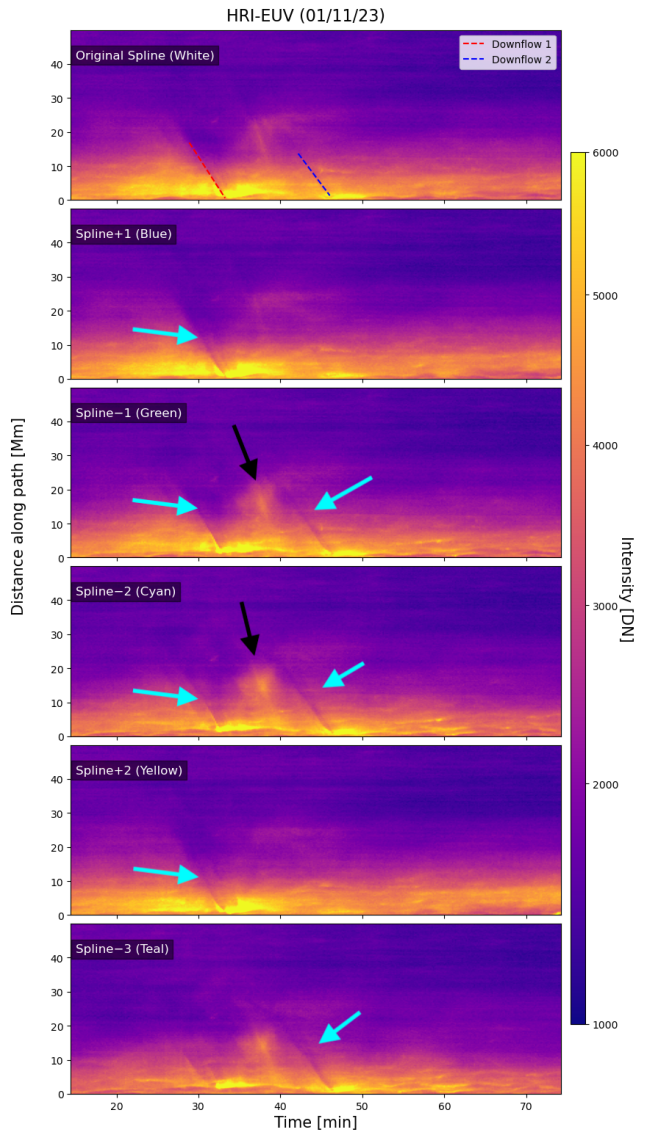


Figure 10. Time-distance diagrams extracted from the cubic splines in Figure 4. Many rain clumps can be seen, notably those signaled by the cyan arrows, denoted as ‘downflow 1’, occurring between $t = 28 - 35$ min (red dashed segment in the top panel), and ‘downflow 2’, between $t = 42 - 48$ min (blue dashed segment in the top panel). The black arrow indicates the presence of an upward flow (see Figure 18).

From the time-distance diagrams in Figure 10, we choose the white spline to calculate the speeds of the descending coronal rain based on visual clarity. The first clump denoted as downflow 1 in HRI_{EUV}, descends at a constant projected speed of approximately 62.0 ± 10.0 km s⁻¹. The rain is seen in absorption, with emission ahead of the rain increasing in intensity as it falls, as expected from compression. Another clear downflowing feature, which we refer to as downflow 2, can be seen in Figure 10 between $t = 42 - 48$ min, which descends at a constant projected speed of 53.3 ± 10.0 km s⁻¹. No clear acceleration or deceleration of the clumps is observed by HRI_{EUV}, suggesting a balance of forces (e.g. gas pressure and gravity) as the rain has reached terminal velocity, as discussed by Oliver et al. (2014). The rain is seen to descend an approximate distance of 60 Mm

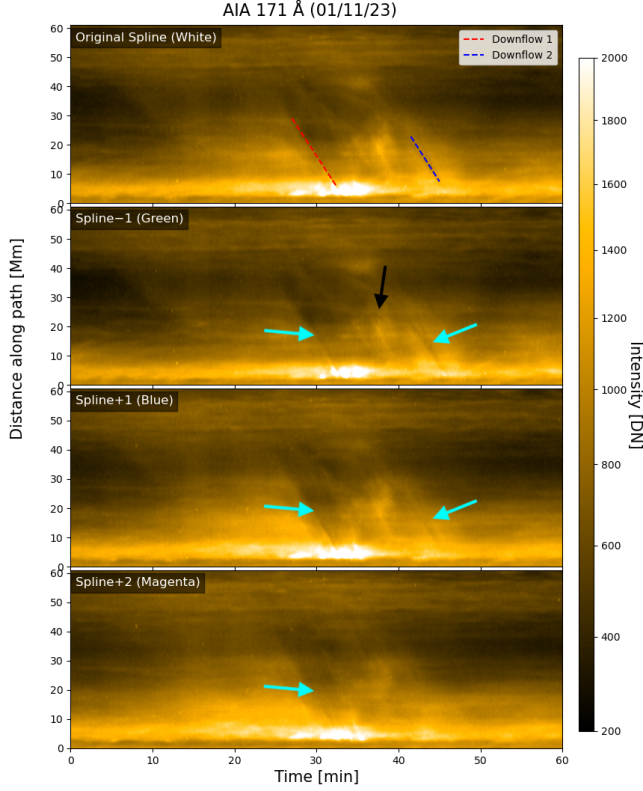


Figure 11. Similar to Figure 10 but for the splines plotted in Figure 5 for AIA 171 Å. downflows 1 and 2, identified in Figure 4, can also be seen here clearly (respectively, red and blue dashed segments in top panel).

but is revealed more clearly in the last 20–30 Mm in the time-distance diagram.

As discussed in 3, we first analysed the trajectory of the coronal rain event in AIA 171 Å and used the same cubic spline coordinates in all other AIA wavelengths. The four cubic splines shown in Figure 5 fully capture the extent of the rain shower from AIA’s perspective. Using these splines we also show in Figures 11 and 12 the time-distance diagrams for AIA 171 Å and 131 Å, respectively, which reveal more details about the rain shower. Indeed, these time-distance diagrams show signatures of more downflows prior to downflow 1, suggesting that the rain shower may start at $t \approx 5$ min from the start of the observation and may last for roughly 35 min. As with HRI_{EUV}, we also note the presence of the compression ahead of the rain in the last few Mm, as well as signatures of the ‘fireball’ effect immediately beneath the rain.

Downflow 1 can be seen in 131 Å, 171 Å, 193 Å, and 211 Å, but not AIA 94 Å and 335 Å. Across these wavelengths, downflows 1 and 2, fall with the same constant projected speeds of $71.2 \pm 10.0 \text{ km s}^{-1}$ and $73.6 \pm 10.0 \text{ km s}^{-1}$ respectively, with no signatures of acceleration or deceleration. The constancy in the speeds indicates that temperature does not affect the observed speeds, as is expected from coronal rain.

In Figure 13 we show the time-distance diagram for AIA 304 Å, which is adept to cooler temperatures of $\log T \approx 5$ characteristic of the low transition region. We can see two large absorption features at 50–60 Mm, matching the expected starting times of downflows 1 and 2 seen in the hotter wavelengths lower down the loop. These clumps can be seen throughout the fall, but with more or less clarity depending on the brightness of the background (the clumps can either absorb or emit stronger than the background).

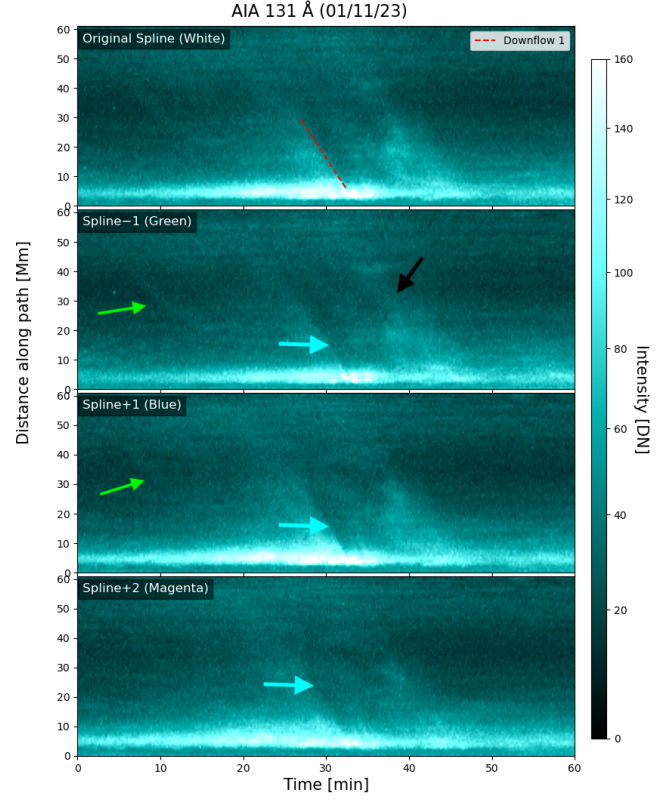


Figure 12. Similar to Figure 10 but for AIA 131 Å with the splines plotted in Figure 5. Note the presence of more downflow signatures prior to downflow 1 (indicated by the green arrows).

AIA 131 Å, 171 Å and HRI_{EUV}, presented a clear EUV enhancement likely due to compression ahead of the descending rain, followed by absorption. In contrast, AIA 193 Å and 211 Å primarily showed a large absorption feature without the EUV enhancement ahead. This suggests that the compression due to descending coronal rain is in a temperature range of 0.4–1 MK. This is confirmed by the DEM analysis shown in Figure 14, which shows significant emission only in the temperature range of $\log(T) = 5.5 - 6.15$.

By analysing the absorption created by the rain in Figure 10 we estimated the length of downflow 1 to be 1.1 ± 0.3 Mm. This length could be much longer [Antolin & Rouppe van der Voort](#) (as seen in previous rain observations, e.g. 2012), but not producing enough absorption to be observed. However, we believe that downflow 1 is a collection of smaller, unresolved clumps (as seen in AIA 304 Å) and to obtain a more accurate length, we multiplied the total velocity over the time between downflow 1 and the beginning of the upward flow (equal to 120 s, which matches the time interval where most of the enhanced brightening is observed in the impact region). This leads to a length of 8.7 ± 1.2 Mm.

4.2.2 Total rain speed

Using the projected velocities of downflows 1 and 2 from the two LOS provided by HRI_{EUV} and AIA in Figures 10 and 11, we calculated the total velocities with the following equations. First, the separation angle between AIA and HRI_{EUV} is:

$$\theta_{EA} = \theta_{EUV} + \theta_{AIA}, \quad (5)$$

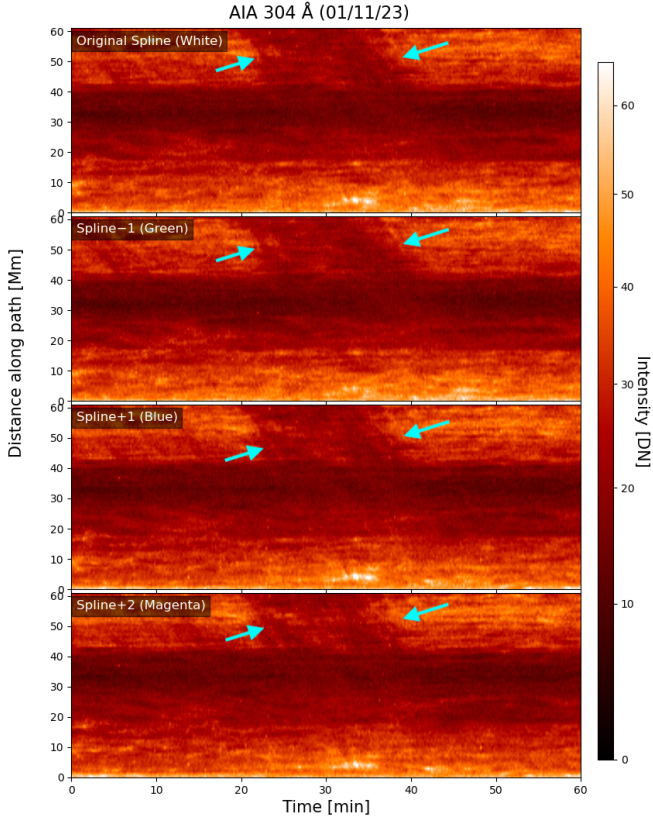


Figure 13. Similar to Figure 11 but for AIA 304 Å using the splines plotted in Figure 5. The left cyan arrows point to a large absorption feature observed near the apex of the loop, which corresponds to the clump formation occurring between $t = 22 - 35$ min leading to downflow 1. The right cyan arrow indicates downflow 2. Note the presence of further downflow signatures prior to downflow 1, also observed in Figure 12 with AIA 131 Å.

where θ_{EUI} and θ_{AIA} denote, respectively, the separation angles between the plane-of-the-sky (POS) of HRI_{EUV} and the coronal rain path, and between the POS of AIA and the coronal rain path. The projected velocity of the coronal rain in the POS of HRI_{EUV}, v_{EUI} is related to the total velocity v as:

$$v_{\text{EUI}} = v \cos(\theta_{\text{EUI}}). \quad (6)$$

Similarly, the velocity of the rain in the AIA's POS is:

$$v_{\text{AIA}} = v \cos(\theta_{\text{AIA}}). \quad (7)$$

These equations can be combined to obtain the total velocity v :

$$v = \pm \sqrt{\left(\frac{v_{\text{AIA}} - v_{\text{EUI}} \cos(\theta_{\text{EA}})}{\sin(\theta_{\text{EA}})} \right)^2 + v_{\text{EUI}}^2}. \quad (8)$$

The separation angle between Solo and AIA was obtained from the Stereo Science Centre website ([online](#)), where $\theta_{\text{EA}} = 0.35$ rad. Taking the speeds of downflow 1 to be $v_{\text{AIA}} = 71.2 \text{ km s}^{-1}$ and $v_{\text{EUI}} = 62.0 \text{ km s}^{-1}$, we get a total velocity of $v = 72.5 \text{ km s}^{-1}$. Similarly, for downflow 2 we have $v_{\text{AIA}} = 73.6 \text{ km s}^{-1}$ and $v_{\text{EUI}} = 53.3 \text{ km s}^{-1}$, we get a velocity of $v = 86.4 \text{ km s}^{-1}$.

4.3 Compression by the rain

We now analyse the compression produced by the rain during the fall and show that the ratio of specific heats (and polytropic index) can

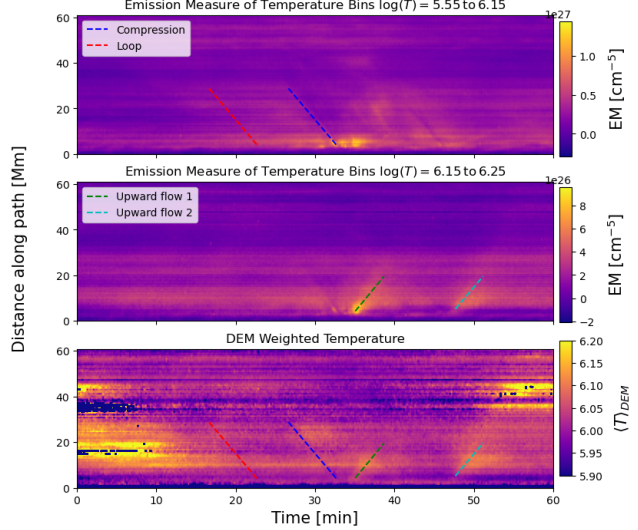


Figure 14. The top panel shows the total emission measure (EM) in the temperature range $\log(T) = 5.5 - 6.15$. The blue dashed line follows the compression by the rain. The red dashed line represents a parallel in time and space to the blue line, prior to the main rain event (downflow 1). Only temperature bins corresponding to $\log(T) = 6.15$ and 6.25 depicted the rebound flows. We denote 'Rebound 1' in green, and 'Rebound 2' in cyan in the middle panel. The bottom panel shows the DEM weighted temperature, where the loop, compression (due to downflow 1) and rebound flow lines are plotted.

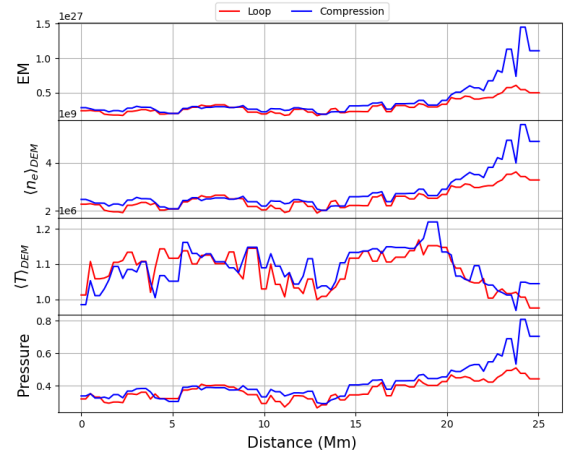


Figure 15. Thermodynamic quantities along the red (denoted as 'loop' conditions) and blue (corresponding to compression) lines in Figure 14. We show the emission measure (EM, top panel), the electron number density (Eq. 4, second from top), the DEM weighted temperature (Eq. 3, third from top), and the pressure (bottom).

be estimated from it. For this, we first calculate the electron number densities and DEM-weighted temperatures in the compressed plasma. Using the methods described in Section 3 we calculate these quantities along the blue and red lines in Figure 14, which follow, respectively, the compression produced by the rain and the parallel to this at a time 10 min prior, when the rain compression is not ob-

served (but the conditions in the loop are otherwise assumed to be very similar). We denote the latter conditions (from the red line) as the ‘loop’ conditions (without rain compression). The result is shown in blue in Figure 15.

Because of the relatively low efficiency of thermal conduction in the compressed region (the energy cannot be conducted upwards due to the presence of the rain acting like a cork), and a low loss through radiation due to the relatively small time interval, we can assume the compression to be adiabatic, which implies:

$$T_c n_{e,c}^{-\gamma+1} = T_l n_{e,l}^{-\gamma+1}, \quad (9)$$

where T_c and T_l denote, respectively, the compression and loop temperatures obtained from the DEM-weighted temperature. Similarly, $n_{e,c}$ and $n_{e,l}$ denote the electron number densities of the compression and of the loop, respectively, obtained from equation 4. γ denotes the ratio of specific heats. We then have:

$$\gamma = 1 - \frac{\ln\left(\frac{T_c}{T_l}\right)}{\ln\left(\frac{n_{e,l}}{n_{e,c}}\right)}. \quad (10)$$

To calculate the electron number density we took l in Equation 4, as the width of the observed compression. We obtained a compression width of 0.557 ± 0.01 Mm observed in HRI_{EUV} and 0.690 ± 0.01 Mm observed in AIA 171 Å. The larger compression width in AIA is likely due to the instrument’s lower spatial resolution. Therefore, we used for l the width obtained in HRI_{EUV}.

For the compression values of density and temperature, we choose the point of maximum compression seen in Figure 15. Using this location in time and space, we take the number density of the loop at the same height but 10 minutes before (along the red line in Figure 14). This leads to a value of $T_c = (1.04 \pm 0.05) \times 10^6$ K, $n_{e,c} = (5.59 \pm 0.19) \times 10^9$ cm⁻³, $T_l = (1.00 \pm 0.09) \times 10^6$ K, $n_{e,l} = (3.43 \pm 0.16) \times 10^9$ cm⁻³. We then obtain $\gamma = (1.085 \pm 0.218)$, reflecting the isothermal behaviour during the compression seen in Figure 15 and the reionisation of the neutral plasma in the rain.

4.4 Rain Impact on the Lower Atmosphere

To assess the impact of coronal rain on the lower atmosphere, we created a specific area at the footpoint of the loop known as the ‘Impact Region’ in Figures 4 for HRI_{EUV} and 5 for AIA. We verified that the selected region consistently covered the impact of the descending coronal rain across all the AIA wavelengths. The impact is also seen in SJI 1400 Å and AIA 304 Å, suggesting that the rain reaches, at least, the lower layers of the transition region.

We summed the intensity values within these regions and plotted the light curves in Figure 16. The light curves present a consistent pattern across multiple wavelengths, with an increase and simultaneous peak in intensity at around $t = 30 - 35$ min, matching the time of impact of downflow 1, followed by a sharper decline. This is consistent across all the AIA EUV wavelengths, the HRI_{EUV} and the SJI 1400 Å. The increase and decrease trends are different across the wavelengths. The increase can be initially slow (over 30 min as seen in AIA 211 Å), or fast (lasting only 5 min in AIA 94 Å), and probably reflects the different processes at play, achieving different temperatures at different times. For instance, the intensity rise over ≈ 20 min seen in AIA 171 Å, 131 Å and HRI_{EUV} match the timescale over which compression is seen in the time-distance diagrams (and correspondingly, the intensity decline after the impact is sharper in these wavelengths). A second smaller intensity increase can be seen

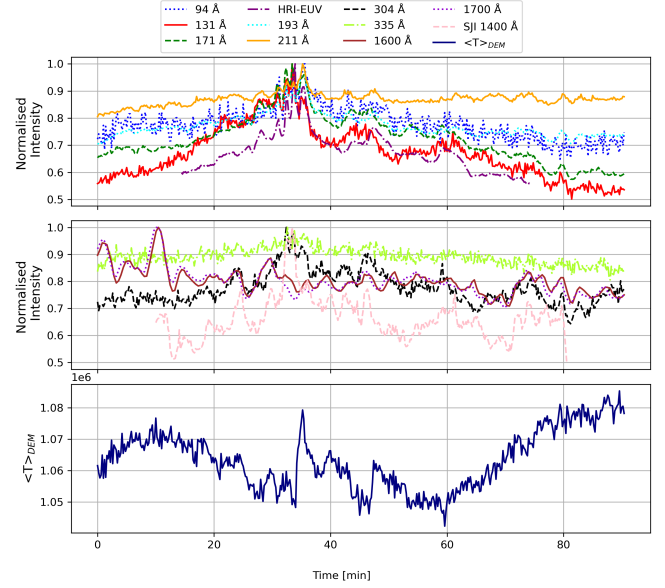


Figure 16. Multi-wavelength emission from the impact of coronal rain in the lower atmosphere (top and middle panel). Co-alignment of UT times has been taken into account, and the time it takes light to travel to HRI_{EUV} compared to AIA and SJI. We see a peak at around $t = 30 - 35$ min in all intensities (except for AIA 1600 Å), suggesting that the rain impacts deep into the lower transition region and compresses the plasma. The DEM-weighted temperature of the impact region is plotted in the lower panel.

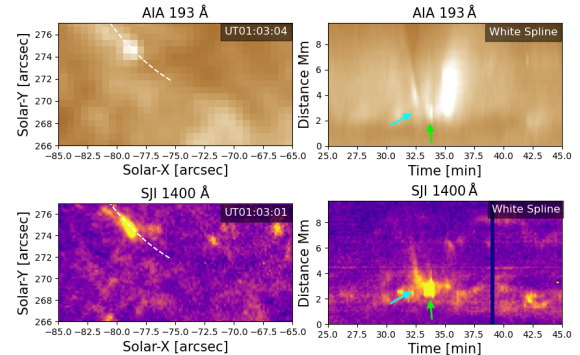


Figure 17. Rain impact detected by AIA and SJI. Left column: snapshot of AIA 193 Å (top) and SJI 1400 Å (bottom) immediately prior to impact, where the white cubic spline denotes the trajectory of the rain clump. Right column: the corresponding time-distance diagrams along the white cubic spline in AIA (top) and SJI (bottom). The time-distance diagrams clearly shows the impact of downflow 1 (cyan arrow) with smaller clumps impacting after (green arrow). The rebound flow can only be seen in the AIA 193 Å time-distance diagram. See the online animation corresponding to this Figure.

at $t \approx 45 - 47$ min, and likely corresponds to downflow 2 since the timing matches the expected impact from the time-distance diagrams.

AIA 1600 Å and 1700 Å exhibit no noticeable intensity variation around the times of the impacts. Hence, the rain does not seem to reach the chromosphere.

We calculated the DEM weighted temperature for the impact region and plotted it in the bottom panel of Figure 16. We notice very small variation on the order of 20 – 30 kK over the entire observa-

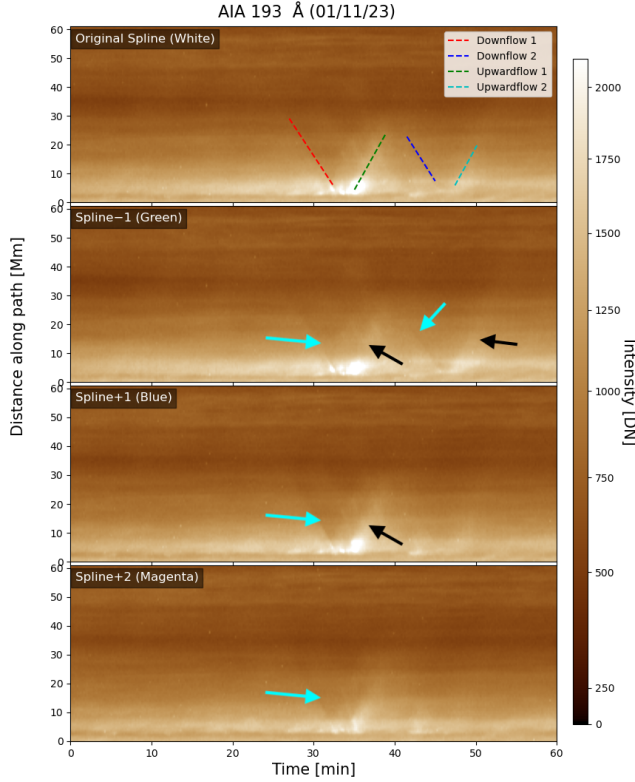


Figure 18. Similar to Figure 4 but for AIA 193 Å with the splines plotted in Figure 5. The cyan arrows point to the descending clumps, while the black arrows point to the rebound flows. The speeds of the rebound flows are calculated using the green dashed lines (top panel).

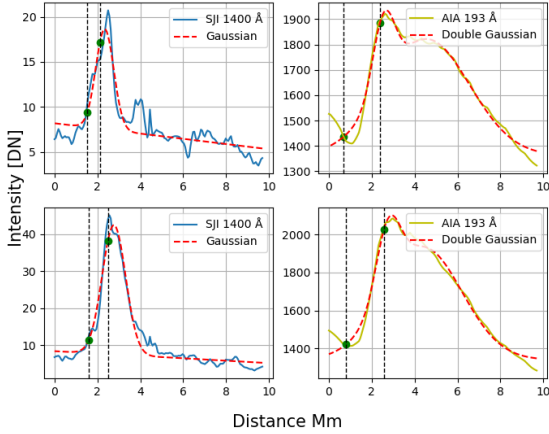


Figure 19. The top and bottom rows show average intensities for SJI 1400 Å (left) and AIA 193 Å (right) prior and during impact, respectively. The averages are done with the time-distance diagrams of Figure 17 over the time interval 30.5 – 31.5 min (prior to impact) and 33 – 34 min (during impact).

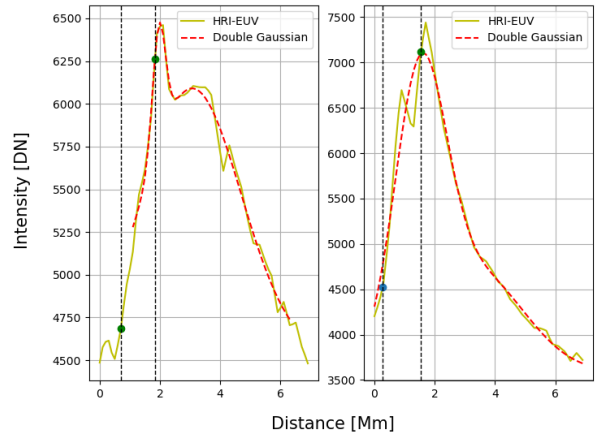


Figure 20. Similar to Figure 19 but for HRI-EUV. The average intensity was obtained with the time-distance (white spline) diagram of Figure 10 over the time interval 30.5 – 31.5 min (prior to impact) and 33.5 – 34 min (during impact).

tion, reflecting the isothermal behaviour of the compression ahead of the rain seen in Figure 15. The temperature actually exhibits a small decrease over the time of the impact of downflow 1, followed by a sharp peak of ≈ 30 kK matching the time of the rebound flow (discussed in the next section). A second smaller peak of ≈ 10 kK can be seen at $t \approx 45 - 47$ min, which matches the time the rebound flow from downflow 2. This is then followed by a steady increase of 30 kK after $t = 60$ min, which may suggest reheating of the loop and the start of a new TNE-TI cycle.

In Figure 17 we take a close loop at the impact region as seen in AIA 193 Å and SJI 1400 Å. We note that the trajectory of the rain is slanted at the footpoint, indicating a similar topology for the magnetic field. Several small brightening events can be seen accompanying the impact of downflow 1, with an overall intensity enhancement over 2 – 3 min (see also online animation). We notice the presence of the subsequent upflow following the rain impact in AIA 193 Å but not in the IRIS channel, which we examine in the next section. We also notice that prior to the downflow 1 a more continuous (with little variability) intensity enhancement can be seen in both channels. This ‘steady’ intensity enhancement can be seen in the full time-distance diagram of Figure 18 and in basically all the other channels. We note that the region in both channels at the base of the loop and underneath the impact region is dark.

To compare more closely the observed intensity variability across the channels we plot in Figure 19 a time average over 1 min prior ($t = [30.5 - 31.5]$ min) and during the impact ($t = [33 - 34]$ min) for the intensities seen in the time-distance diagrams. Both the ‘steady’ intensity enhancement and that from the impact can be seen as very similar large bumps in the intensity profiles (with an increased value for the impact). We measure the widths of these enhancements by fitting a single or double Gaussian over the profile, as shown in the Figure. The SJI profiles prior and during the impact can be fitted with a single Gaussian with a FWHM of 0.98 Mm and 1.29 Mm, respectively. Similarly, AIA can be fitted with a double Gaussian, with a narrow (first) component’s FWHM of 1.18 Mm and 1.30 Mm, respectively, prior and during impact. The broad (second) component of the fit has a FWHM of 4.76 Mm and 4.25 Mm, respectively, prior and during impact. We repeat this measurement for HRI-EUV using

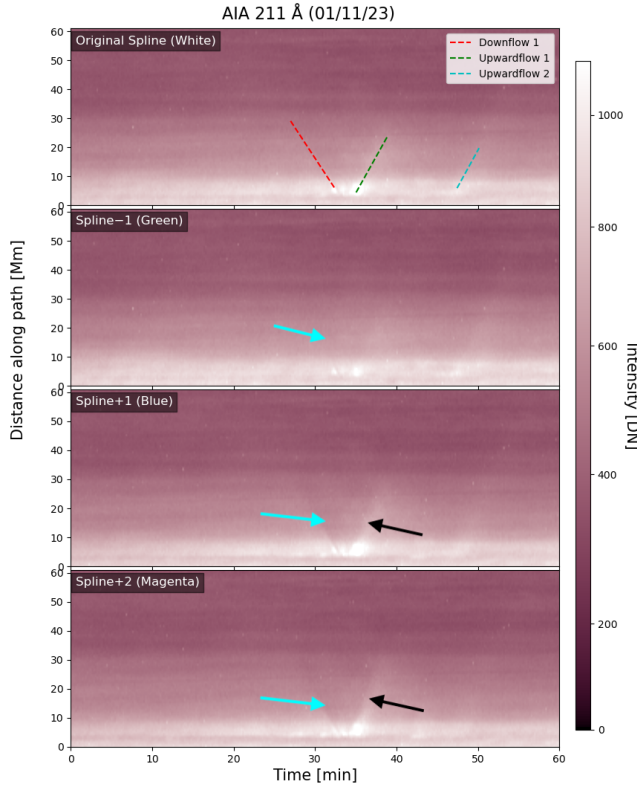


Figure 21. Similar to Figure 4 but for AIA 211 Å with the splines plotted in Figure 5. The cyan arrow points to downflow 1, while the black arrow points to the rebound flow. The speed of the rebound flow is calculated using the green dashed line (top panel).

the time-distance diagram of Figure 10, and we show the resulting intensity profile and Gaussian fit in Figure 20. Also for this case, the intensity profile is best fitted by a double Gaussian. Prior to impact, the narrow (first) component has a FWHM of 0.58 Mm, and the broader (second) component has a FWHM of 3.83 Mm. In contrast with the AIA and SJI profiles, during the impact the HRI_{EUV} intensity profile is more significantly affected. The widths of the narrow and broad components then become 2.0 Mm and 3.77 Mm. These changes could be due to the change in the LOS.

The widths of both the narrow and broad components for SJI 1400 Å HRI_{EUV} and AIA 193 Å are very similar, implying that the heating (either steady, prior to impact) or impulsive (during impact), affects the entire transition region. The transition region is naturally narrower in SJI 1400 Å compared to AIA 193 Å, but it is interesting that it is even narrower in HRI_{EUV}, in agreement with the results of Mandal et al. (2023) where the studied dynamic fibrils with HRI_{EUV} appear to show a bright front with a thickness of less than 1 Mm. The different LOS of HRI_{EUV} could also affect the observed width. The fact that during impact, the AIA 193 Å and SJI 1400 Å intensity enhancements (which share the same LOS) are observed at the same height in both channels suggests no change in the observed impact depth of the coronal rain clumps in SJI 1400 Å compared to AIA 193 Å further indicating that the entire transition region is affected by the impact. The persistent narrow bump observed in HRI_{EUV}, and AIA 193 Å (and in many other AIA channels) could be interpreted as a footpoint localised steady heating component, as expected by TNE theory. To have a measure of the width of this transition we measure the thickness from 10% the peak of the Gaussian

fits to 10% the background value on the left side of the Gaussian fits (this is marked by the green points in each Panel of Figures 19 and 20). In the case of AIA and HRI_{EUV}, we do this with the Gaussian fit on the small bump, since this is the one located lower in the atmosphere. We find values for SJI 1400 Å of 0.61 Mm and 0.92 Mm prior and during impact, respectively. Similarly, for HRI_{EUV} we find 1.14 Mm and 1.28 Mm. Finally, for AIA 193 Å we find 1.71 and 1.77 Mm.

4.5 Rebound Flow

After the impact of downflow 1, a clear upward propagating feature originating from the impact region, termed ‘upward flow 1’, was identified between $t = 34 - 37$ min in AIA 193 Å and AIA 211 Å, respectively, in Figures 18 and 21. A second upward propagating feature can be seen (best in AIA 193 Å) between $t = 44 - 48$ min (‘upward flow 2’), following the impact of downflow 2. Upward flow 1 has constant projected speed of 83.6 ± 10.0 km s⁻¹ in both AIA 193 Å and 211 Å. Similarly, upward flow 2 has a constant projected speed of 85.0 ± 10.0 km s⁻¹ in AIA 193 Å. Both rebound flows occur almost instantly following the impact of the descending coronal rain. Hence, we interpret these propagating features as rebound flows because of the relatively low speeds compared to the sound speed.

The fact that we observe these upflows very clearly in AIA 193 Å and 211 Å indicates relatively hot temperatures reaching 1.25–2 MK. This is supported by the DEM analysis in Figure 14, which shows that only temperature bins corresponding to a temperature range of $\log(T) = 6.15$ to 6.25 revealed the rebound flow. Upon close inspection, other wavelengths such as AIA 94 Å, 131 Å, 171 Å, and HRI_{EUV}, also show signatures (but less distinct) of these upward flows denoted by the black arrows in the respective time-distance diagrams. The distance along the loop the upflows are seen to reach in both the AIA 193 Å and 211 Å is approximately 58 ± 3 Mm. 53.3 ± 10 km s⁻¹ Using the projected and total velocity of downflow 1 and rearranging equation 7, we obtain $\theta_{AIA} = 0.19$ radians. Using this, we can calculate the total velocity of upward flows 1 and 2 in Figure 18. Taking the projected velocity of upward flow 1 to be 83.6 km/s, we get a total velocity of 85.2 km/s. Taking the projected velocity of upward flow 2 to be 85.0 km/s, we get a total velocity of $v = 86.5$ km/s.

Using AIA 193 we estimated the width of upward flow 1 using the FWHM to be 0.86 ± 0.007 Mm. We further estimated the length using Figure 18 to be 7 ± 0.5 Mm. Upward flow 2 is not seen as clearly in order to accurately calculate the width.

4.6 Energy Estimate

We can now estimate the kinetic energy of the rain clump, $K_e = \frac{1}{2}mv^2$, where m and v denote, respectively, the rain clump’s mass and total velocity. For this, we must first calculate the electron number density of the clump, which is determined assuming pressure balance between the rain clump and the compression ahead of the rain. We can also assume that the temperature of the clump is on the order of 10^4 K (and probably less), given that it produces EUV absorption (due to neutral hydrogen and helium, and singly ionised helium).

We obtain an electron number density for the clump of $(5.86 \pm 0.37) \times 10^{11}$ cm⁻³, which is in line with usually reported density values for coronal rain (Antolin & Froment 2022). Based on the rain volume (assuming cylindrical geometry), and using the morphological properties mentioned in section 4.2.1 and observed total

descending speeds calculated in section 4.2.2, we obtain a kinetic energy for the rain clump of $(6.19 \pm 2.04) \times 10^{25}$ erg.

We also calculate the thermal and kinetic energy of the rebound flow to analyse how much energy from the rain clump is transferred to it. The former is given by $U = \frac{3}{2}k_B V T n_{\text{tot}}$, where V , T and n denote, respectively, the volume, temperature and number density of the upflow. Using the values for the upward flow found in section 4.5 we find thermal and kinetic energies of $(1.01 \pm 0.25) \times 10^{24}$ erg and $(9.24 \pm 0.8) \times 10^{24}$ erg, respectively. We notice a factor of more than 10 difference between these values and the rain clump energy.

The rain impact will also likely generate MHD waves, and particularly slow modes. Such modes would propagate upward at the sound speed. Although they do not show up in the time-distance diagrams, it is useful to estimate their kinetic energies. These are well approximated by $E_w = \frac{1}{2}\rho(\delta v)^2 c_s$, where δv is the amplitude and c_s is the sound speed. Since we do not observe the slow modes we can assume a maximum amplitude of 10% the sound speed. We also assume the same volume as for the flow and obtain a wave kinetic energy value of 3.9×10^{22} erg, which is negligible compared to the flow energy.

We therefore find that less than 20% of the clump's kinetic energy is transferred to the rebound flow. Since the impact is seen across all EUV and UV wavelengths (except AIA 1600 and 1700) we can deduce that most of the energy is radiated away in the transition region upon impact. For convenience we summarise all calculated values in Table 1.

5 DISCUSSION AND CONCLUSION

This study provides a multi-wavelength observation of quiescent coronal rain and its effects on the lower and upper atmosphere with the help of instruments such as HRI_{EUV}, AIA and IRIS/SJI. The coronal rain is observed on disc and is seen to fall onto a leading polarity region. The loop hosting the rain has both footpoints anchored in moss, where small and rapid EUV intensity enhancements are observed with HRI_{EUV}, similar to those reported by Berghmans et al. (2021). We analysed the dynamics of the rain, its impact in the lower atmosphere and the morphological changes of the coronal loop that appear related to the rain.

Throughout the entirety of the event, we observed strong EUV variability both during the rain shower (where downflows 1 and 2 are observed) and after its impact on the lower atmosphere. At the start of the observation, the coronal strands appeared densely packed and uniform in intensity, and by the end of the observation, we observed multiple strands disappearing with new ones appearing and notable gaps between strands. Such EUV variability is in agreement with that reported from loops in TNE-TI (Antolin et al. 2023), also in line with the generally observed variability in coronal loops (Ugarte-Urra et al. 2006; Antolin & Froment 2022).

Although only two main clumps were very clearly detected (with EUV absorption signatures in HRI_{EUV}), there appeared to be multiple smaller clumps falling, consistent with a large shower. This is supported by the streaks of lines prior to downflow 1 in HRI_{EUV} and AIA (131 Å, 171 Å and 304 Å) time-distance diagrams, and also during downflows 1 and 2 (observed in all time-distance diagrams). Overall, the rain shower appears to last about 35 min. The total length of the loop is approximately 160 Mm with the clump being observed to fall approximately 58 Mm. As depicted in the time-distance diagrams, only the last 20 – 40 Mm reveals the clumps clearly. All EUV-UV channels, except from AIA 1600 Å and 1700 Å, detect the descending clump and the impact as depicted by figure 16. This

supports coronal rain clumps being multi-thermal as discussed in Antolin et al. (2015). This is further supported by the DEM analysis in 4.3 where we detect the presence of coronal rain in temperature bins 0 – 7, which have a temperature range of $\log(T) = 5.5 – 6.25$.

The main coronal rain clump produced EUV absorption, with compression occurring ahead of the rain, particularly strong in the last minute prior to impact (up to a height of ≈ 3 Mm). The width of this compression is almost exactly the same as that of the rain width, reflecting the low plasma β conditions and field-aligned motion of the plasma. Indeed, the 2D MHD numerical simulations by Martínez-Gómez et al. (2020) show different compression and dynamics (with Kelvin-Helmholtz instability vortices at the wake of the rain) in the case of high plasma β . An additional brightening due to compression and heating immediately below the condensations is also observed at high resolution with HRI_{EUV}, which is consistent with the ‘fireball’ effect first detected by Antolin et al. (2023). Signatures of this effect can also be seen in some of the AIA passbands.

Using the separation angle between AIA 171 Å and HRI_{EUV} at the time, we were able to calculate the total rain speed of downflows 1 and 2 to be 72.5 ± 10.0 km s⁻¹ and 86.4 ± 10.0 km s⁻¹, respectively. No clear acceleration or deceleration was observed, suggesting a balance of gas pressure and gravity. The speeds obtained are in agreement with previous studies (De Groot et al. 2005; Antolin & Rouppe van der Voort 2012; Ishikawa et al. 2020). These dynamics are likely linked to the observed intensity brightening ahead of the rain suggesting compression. Compression from coronal rain (or prominence downflow) has been analysed analytically and numerically (Mackay & Galsgaard 2001; Adrover-González et al. 2021), predicting deceleration or piston-like oscillations around nodal points along the loop. Oliver et al. (2014) have demonstrated that the abrupt formation of a condensation generates sound waves upstream and downstream, that modify the pressure as they travel and effectively decelerates the clump and leads to a constant velocity during most of the downfall. Recently, this effect has been explained by Hillier et al. (2025) as a dynamic mass contribution from the compressed material ahead of the rain, which then modifies the momentum of the rain.

Based on the EUV absorption feature observed by HRI_{EUV}, we calculated the width of downflow 1 to be 549 ± 27 km. This width falls in line with those found with the same instrument at similar resolution by (Antolin et al. 2023), and off-limb with SJI 2796 Å, 1400 Å, and 1330 Å at similar resolution with IRIS by (Antolin et al. 2015), strengthening the previous result that coronal rain widths are independent of temperature. As in Sahin et al. (2023), the width of the clump was observed to be constant along the loop's length. This property remains unexplained, and may be attributed to the fundamental scales over which coronal heating operates Antolin & Froment (2022) and/or to the pressure balance that follows thermal instability.

The length of the EUV absorption feature created by downflow 1 is 1.1 ± 0.3 Mm, which is similar to the width of the cool (chromospheric) coronal rain core found in the numerical simulations by (Antolin et al. 2022). The actual length of the coronal rain clump (extending to higher transition region temperatures) is most likely greater as the tail can be elongated (Fang et al. 2013). Also, we believe that downflow 1 is a collection of clumps, as suggested by the features seen in AIA 304 Å. To refine our length estimate, we multiplied the speed of downflow 1 by the time interval between the impact and the onset of the upflow (matched by the continuous intensity enhancement observed during that time), to obtain a value of 8.7 ± 1.2 Mm. The studies referred to above report a broad distribution of rain lengths, from a few Mm up to 20 Mm. Fang et al.

Parameter	Downflow 1	Upward Flow 1	Compression
Temperature T (K)	10^4	$(1.63 \pm 0.07) \times 10^6$	$(1.04 \pm 0.06) \times 10^6$
Electron density n_e (cm^{-3})	$(5.86 \pm 0.37) \times 10^{11}$	$(3.50 \pm 0.06) \times 10^9$	$(5.59 \pm 0.19) \times 10^9$
Pressure (dyn cm^{-2})	0.81 ± 0.05	0.79 ± 0.04	0.81 ± 0.05
Velocity (km/s)	72.5 ± 10.0	85.2 ± 10.0	–
Width (km)	549 ± 27	862 ± 7	–
Length (km)	8702 ± 1200	7000 ± 500	–
Kinetic Energy (erg)	$(6.19 \pm 2.0) \times 10^{25}$	$(1.01 \pm 0.25) \times 10^{24}$	–
Thermal Energy (erg)	$(4.69 \pm 0.86) \times 10^{24}$	$(9.24 \pm 0.8) \times 10^{24}$	–

Table 1. Physical quantities for downflow 1, upward flow 1, and the compression occurring ahead of the downflow 1.

(2015) found that coronal rain lengths are subjected to shear flows, gas pressure and gravity as they descend.

Based on the observed compression produced by the rain, we calculated the ratio of specific heats and obtained a value of $\gamma = 1.085 \pm 0.218$. This is based on the assumption that the compression occurs adiabatically, based on the short time interval (minutes) and length scale (less than 10 Mm) of the process. The rain effectively stops thermal conduction to transfer energy upstream, limiting the energy loss to radiation, which should be small due to the short timescale. The low γ value indicates an isothermal compression. Low γ values have been reported previously by Van Doorsselaere et al. (2011), who found $\gamma = 1.10 \pm 0.02$. However, they observe a warm, highly ionised coronal loop using spectroscopic data from Hindoe/EIS, and therefore interpret their results based on a very strong thermal conduction. Similarly, Prasad et al. (2018) also report low γ values. Their research studied 30 active region loops using a DEM analysis and found a temperature dependence on γ , with cooler coronal loops exhibiting lower values. Vashalomidze et al. (2019) calculate γ at the time of coronal rain onset, and found values of 2.1 ± 0.11 , which they interpret as signatures of thermal instability. In our case, a γ value close to 1 suggests the presence of molecules. The EUV absorption already indicates the presence of neutral hydrogen and helium and therefore temperatures likely under 10,000 K. Based on the spectral line width of $\text{H}\alpha$ with SST observations, Antolin et al. (2015) find upper thresholds for the rain temperatures of 5000 K. Mulay & Fletcher (2021) and Mulay et al. (2023) have found molecular H_2 emission in flare ribbons and jets, indicating temperatures around 4000 K. Hence, it is possible that molecules such as H_2 are also formed in coronal rain.

We also detect upward motions that follow the impact of downflows 1 and 2. Rebound flows and shocks produced by the rain's impact have been reported first by Antolin et al. (2023) with HRI_{EUV} . In our case, the upward motions are only clearly observed in the AIA 193 Å and 211 Å passbands, indicating temperatures of $\log T = 6.1 - 6.3$, supported by the DEM analysis. The upward motions travel at a constant total velocity of $(85.1 - 86.5) \pm 10.0 \text{ km s}^{-1}$. Since these speeds are much lower than the sound speed we interpret them as hot rebound flows, which then start to reheat the loop, indicating the start of a new TNE-TI cycle. Such atmospheric responses are expected from numerical simulations (e.g. Müller et al. 2003; Antolin et al. 2022). These upward motions can be traced clearly up to the formation height of downflow 1. The upflows are seen only about a minute after the downflow impact, further supporting the presence of multiple clumps accompanying downflows 1 and 2. The widths of upflow 1 is ≈ 860 km, significantly larger than the rain width. This could be explained by the lower spatial resolution of AIA. However, an additional effect may contribute to these relatively large widths. It is plausible that the rain's impact generates transverse magnetic perturbations in the low transition region, due to the higher plasma β

at those heights, which, in turn, should generate compression in the neighboring field lines, leading to upward flows in a wider volume than that traced by the rain. The future higher resolution observations in hot lines offered by MUSE and EUVST should be able to confirm this hypothesis.

One of the most visible effects of the rain in the present case is its impact on the lower atmosphere. The rain shower, composed of small clumps, produces strong and rapid variability on the order of minutes observed in all AIA EUV channels, in HRI_{EUV} and the SJI 1400 Å channel. Reale et al. (2013) report prominence fallback from very large heights to produce similarly strong intensity brightenings across all EUV wavelengths. However, they also report emission in the AIA UV (low chromospheric) wavelengths, which are likely due to the higher falling speeds (up to 450 km s^{-1} , probably due to the negligible effect of the magnetic field in their case) and consequently larger kinetic energies. The strong brightenings we observe are accompanied by a more steady and lower intensity enhancement over tens of minutes, matching roughly the duration of the rain shower, visible in AIA 131 Å, 171 Å and HRI_{EUV} . This variation of intensity is likely due to the inhomogeneity present in the rain. The fact that the impact is seen in SJI 1400 Å indicates that the condensations reach the low transition region. The width and location of the brightening caused by the impact is very similar between SJI 1400 Å, HRI_{EUV} and AIA 193 Å, which suggests that the transition region thickness is very thin (below ≈ 1200 km), matching predictions from numerical modelling (e.g. Reale 2014). However, in the latter we observe a secondary width enhancement of larger magnitude, indicative of heating.

We estimated the duration of downflow 1 to be ≈ 3 min, with a kinetic energy of $(6.19 \pm 2.0) \times 10^{25}$ erg. We also estimated the rain shower to have a duration of roughly 35 min. However, according to the time-distance diagrams (notably AIA 304 Å), we can see that the bulk of the rain shower lasts 15 min (where the EUV absorption is predominant in AIA 304 Å). Hence, if we assume a roughly similar density, the total energy of the rain shower is roughly 3.09×10^{26} erg, that is, on the order of a microflare. It is very likely that the rain's structure is highly inhomogeneous. In the calculation of the rain's density we assumed a temperature of 10,000 K for the rain (which is likely too high). Finally, the length of the rain is inferred rather than directly observed. In any case, these assumptions should compensate each other to some extent.

The significant energy of the impact explains its visibility in all AIA/EUV wavelengths. We also found that about 20% of the clump's kinetic energy is transferred to the thermal and kinetic energy of the rebound flow, along with a negligible wave energy. Hence, the majority of the energy is radiated away upon impact in the transition region. It is interesting to make the analogy to the 'precipitation limit' feedback mechanism observed at the much larger scales of the intracluster medium (ICM). In that field, cool cores containing

relatively dense and very cold gas are observed to accrete towards the supermassive black holes at the centres of galaxy clusters (Voit et al. 2015). These dense inflows impart momentum to the accretion disks, which power energetic AGN jets that subsequently heat the ICM and can slow down the cooling and cool core generation. Hence, a delicate balance is achieved between the number of cool core accretions and the temperature of the ICM from the AGN jets. These ‘precipitation limit’ cycles with the cool cores are analogous to the TNE cycles with coronal rain found in the solar corona. In this work, this analogy is further extended since we show observationally for the first time that the rebound flow from coronal rain can have a major impact on the hosting coronal loop, not only through increasing the temperature but also modifying its morphology.

Lastly, we observe a continuous intensity enhancement at the footpoint of the loop hosting the rain in SJI 1400 Å, HRI_{EUV} and AIA 193 Å during the entire observation sequence, which could correspond to the previously reported steady character of the moss (Antiochos et al. 2003; Brooks et al. 2009). These intensity enhancements are lower amplitude but have similar widths as those observed during impact, (both the small and the larger heating widths of ≈ 1 Mm and ≈ 4 Mm, respectively). This suggests a steady footpoint heating component of similar heating scale length, which could be the kind predicted by TNE. We can estimate or place a lower bound to the volumetric heating of this component with the following reasoning. The kinetic energy of coronal rain is very likely close to the total integrated volumetric heating from coronal heating over the duration prior to the rain. Although a proper estimation of this hypothesis awaits with numerical modelling, this can be justified by the fact that the footpoint heating in the low corona is partly lost in the transition region being radiated away, but a large part of it goes into producing a mild chromospheric evaporation that increases the coronal density (leading to scaling laws such as RTVS, Serio et al. 1981). Most of this density collapses into the condensation, whose potential energy is then converted into kinetic energy as it falls. If so, we can write:

$$E_{CH} \gtrapprox K_{CR}, \quad (11)$$

where E_{CH} denotes the total integrated coronal heating from the beginning of the TNE cycle in which the coronal rain forms, and K_{CR} is the kinetic energy of the rain shower, estimated to be 3.09×10^{26} erg over its 15 min duration. On the other hand, the coronal heating energy is given by:

$$E_{CH} = \int_0^{\tau_{TNE}} \int_0^{s_H} 2H_{CH} dA dt, \quad (12)$$

where H_{CH} is the unknown, roughly steady volumetric heating rate; s_H is the heating scale length, which we assume to be equal to the prevalent small width of ≈ 1 Mm of the intensity brightening observed in AIA 193 Å, HRI_{EUV} and SJI 1400 Å at the loop footpoint; the factor of 2 is to account for both footpoints assuming similar heating conditions¹; and τ_{TNE} is the period of the cycle. Unfortunately, this observational sequence is not long enough to observe another coronal rain event in the same loop with HRI_{EUV}. However, looking further back in time with AIA 304 Å reveals another coronal rain event in the same loop at 22:00UT on October 31st, that is, roughly 2 hrs prior to the studied event. We can take the area A to be set by the width of the upward flow at the footpoint (assuming a circular cross-section). Then, we have:

¹ Numerical simulations indicate that coronal rain often falls towards the footpoint with lower heating rate due to the lower pressure at the footpoint (Froment et al. 2018)

$$H_{CH} \gtrapprox \frac{K_{CR}}{2As_H\tau_{TNE}}. \quad (13)$$

Replacing by the numerical values, we get a volumetric heating rate $H_{CH} \gtrapprox 2.57 \times 10^{-2}$ erg cm⁻³ s⁻¹. Recently, Ishigami et al. (2024) analysed spectroscopically several coronal loops with Hinode/EIS and found heating scale heights of $s_H = 10 \pm 4$ Mm with a volumetric heating rate of $10^{-2 \pm 0.5}$ erg cm⁻³ s⁻¹. Here we take a much smaller heating scale height, given by the persistent intensity brightening observed at the footpoint. On the other hand, the volumetric heating rate that we find is that we find very close to that reported. Although several other factors can influence TNE and coronal rain formation, this similarity also suggests that the coronal loops studied in Ishigami et al. (2024) may be in a state of TNE. More generally, our study illustrates how coronal rain observations can be used to infer key properties of coronal heating.

ACKNOWLEDGEMENTS

Data are courtesy of Solar Orbiter, SDO and IRIS. Solar Orbiter is a space mission of international collaboration between ESA and NASA, operated by ESA. The EUI instrument was built by CSL, IAS, MPS, MSSL/UCL, PMOD/WRC, ROB, LCF/IO with funding from the Belgian Federal Science Policy Office (BELPSO); Centre National d’Études Spatiales (CNES); the UK Space Agency (UKSA); the Deutsche Zentrum für Luft und Raumfahrt e.V. (DLR); and the Swiss Space Office (SSO). The building of EUI was the work of more than 150 individuals during more than 10 years. We gratefully acknowledge all the efforts that have led to a successfully operating instrument. SDO is a mission for NASA’s Living With a Star (LWS) program. IRIS is a NASA small explorer mission developed and operated by LMSAL with mission operations executed at NASA Ames Research Center and major contributions to downlink communications funded by ESA and the Norwegian Space Centre. This research was supported by the International Space Science Institute (ISSI) in Bern, through ISSI International Team project #545 (‘Observe Local Think Global: What Solar Observations can Teach us about Multi-phase Plasmas across Physical Scales’). All images in this manuscript have been made with Matplotlib on Python (Hunter 2007). This research used version 7.0 of the SunPy open source software package (The SunPy Community et al. 2020).

DATA AVAILABILITY

The Solar Orbiter HRI_{EUV} data used in this article is part of Data Release 6.0 (<https://doi.org/10.24414/z818-4163>), which is publicly available. Similarly, the AIA data and IRIS data are publicly available and available at <https://iris.lmsal.com>.

REFERENCES

Adrover-González A., Terradas J., Oliver R., Carbonell M., 2021, *A&A*, **649**, A142
 Antiochos S. K., Karpen J. T., DeLuca E. E., Golub L., Hamilton P., 2003, *ApJ*, **590**, 547
 Antolin P., Froment C., 2022, *Frontiers in Astronomy and Space Sciences*, **9**, 820116
 Antolin P., Rouppe van der Voort L., 2012, *ApJ*, **745**, 152
 Antolin P., Vissers G., Pereira T. M. D., Rouppe van der Voort L., Scullion E., 2015, *ApJ*, **806**, 81

Antolin P., Martínez-Sykora J., Şahin S., 2022, [ApJ, 926, L29](#)

Antolin P., et al., 2023, *Astronomy & Astrophysics*, 676, A112

Aschwanden M. J., Boerner P., 2011, *The Astrophysical Journal*, 732, 81

Auchère F., Bocchialini K., Solomon J., Tison E., 2014, [A&A, 563, A8](#)

Auchère F., Froment C., Soubrié E., Antolin P., Oliver R., Pelouze G., 2018, [ApJ, 853, 176](#)

Berghmans D., et al., 2021, [A&A, 656, L4](#)

Brooks D. H., Warren H. P., Williams D. R., Watanabe T., 2009, [ApJ, 705, 1522](#)

Brooks D. H., Warren H. P., Ugarte-Urra I., Winebarger A. R., 2013, *The Astrophysical Journal Letters*, 772, L19

Chitta L. P., et al., 2022, *Astronomy & Astrophysics*, 667, A166

De Groof A., Bastiaensen C., Müller D. A. N., Berghmans D., Poedts S., 2005, [A&A, 443, 319](#)

De Pontieu B., et al., 2014, [Sol. Phys., 289, 2733](#)

Dere K., 1994, *Advances in Space Research*, 14, 13

Dere K. P., Landi E., Mason H. E., Monsignori Fossi B. C., Young P. R., 1997, *Astronomy and Astrophysics Supplement Series*, 125, 149

Dere K. P., Del Zanna G., Young P. R., Landi E., 2023, [arXiv e-prints](#)

Edlen B., 1945, *Monthly Notices of the Royal Astronomical Society*, Vol. 105, p. 323, 105, 323

Fang X., Xia C., Keppens R., 2013, [ApJ, 771, L29](#)

Fang X., Xia C., Keppens R., Van Doorsselaere T., 2015, [ApJ, 807, 142](#)

Froment C., Auchère F., Bocchialini K., Buchlin E., Guennou C., Solomon J., 2015, [ApJ, 807, 158](#)

Froment C., Auchère F., Mikić Z., Aulanier G., Bocchialini K., Buchlin E., Solomon J., Soubrié E., 2018, [ApJ, 855, 52](#)

Grotian W., 1934, *Zeitschrift für Astrophysik*, Vol. 8, p. 124, 8, 124

Hannah I. G., Kontar E. P., 2012, *Astronomy & Astrophysics*, 539, A146

Hillier A., Oliver R., Martínez-Gómez D., 2025, [A&A, 696, A231](#)

Hunter J. D., 2007, [Comp. Sci. Eng., 9, 90](#)

Ishigami S., Hara H., Oba T., 2024, *The Astrophysical Journal*, 975, 289

Ishikawa R. T., Katsukawa Y., Antolin P., Toriumi S., 2020, *Solar Physics*, 295, 53

Johnston C. D., Cargill P. J., Antolin P., Hood A. W., De Moortel I., Bradshaw S. J., 2019, [A&A, 625, A149](#)

Kawaguchi I., 1970, *Publications of the Astronomical Society of Japan*, vol. 22, p. 405 (1970), 22, 405

Klimchuk J. A., 2015, *Philosophical Transactions of the Royal Society A: Mathematical, Physical and Engineering Sciences*, 373, 20140256

Klimchuk J. A., 2019, submitted to *Sol. Phys.*

Klimchuk J. A., Luna M., 2019, *The Astrophysical Journal*, 884, 68

Lemen J. R., et al., 2012, [Sol. Phys., 275, 17](#)

Leroy J.-L., 1972, *Solar Physics*, 25, 413

Mackay D. H., Galsgaard K., 2001, *Solar Physics*, 198, 289

Mandal S., et al., 2023, [A&A, 678, L5](#)

Martínez-Gómez D., Oliver R., Khomenko E., Collados M., 2020, [A&A, 634, A36](#)

Mulay S. M., Fletcher L., 2021, [MNRAS, 504, 2842](#)

Mulay S. M., Tripathi D., Mason H., Del Zanna G., Archontis V., 2023, [MNRAS, 518, 2287](#)

Müller D., Hansteen V., Peter H., 2003, *Astronomy & Astrophysics*, 411, 605

Müller D., et al., 2017, *Astronomy & Astrophysics*, 606, A10

Müller D., et al., 2020, [A&A, 642, A1](#)

Oliver R., Soler R., Terradas J., Zaqrashvili T., Khodachenko M., 2014, *The Astrophysical Journal*, 784, 21

Pesnell W. D., Thompson B. J., Chamberlin P. C., 2012, [Sol. Phys., 275, 3](#)

Peter H., et al., 2013, *Astronomy & Astrophysics*, 556, A104

Prasad S. K., Raes J., Van Doorsselaere T., Magyar N., Jess D., 2018, *The Astrophysical Journal*, 868, 149

Reale F., 2014, *Living Reviews in Solar Physics*, 11, 4

Reale F., Orlando S., Testa P., Peres G., Landi E., Schrijver C. J., 2013, [Science, 341, 251](#)

Rochus P., et al., 2020, [A&A, 642, A8](#)

Rouillard A., et al., 2017, *Planetary and Space Science*, 147, 61

Şahin S., Antolin P., Froment C., Schad T. A., 2023, *The Astrophysical Journal*, 950, 171

Serio S., Peres G., Vaiana G. S., Golub L., Rosner R., 1981, [ApJ, 243, 288](#)

The SunPy Community et al., 2020, *The Astrophysical Journal*, 890, 68

Ugarte-Urra I., Winebarger A. R., Warren H. P., 2006, *The Astrophysical Journal*, 643, 1245

Van Doorsselaere T., Wardle N., Del Zanna G., Jansari K., Verwichte E., Nakariakov V. M., 2011, *The Astrophysical Journal Letters*, 727, L32

Van Doorsselaere T., et al., 2020, *Space Science Reviews*, 216, 1

Vashalomidze Z. M., Zaqrashvili T. V., Kukhianiidze V. D., 2019, *Astrophysics*, 62, 69

Voit G. M., Donahue M., Bryan G. L., McDonald M., 2015, [Nature, 519, 203](#)

Waters T., Stricklan A., 2024, [arXiv e-prints, p. arXiv:2408.15869](#)

Williams T., et al., 2020, *The Astrophysical Journal*, 892, 134

Şahin S., Antolin P., 2022, [ApJ, 931, L27](#)

van der Holst B., Sokolov I. V., Meng X., Jin M., Manchester IV W. B., Toth G., Gombosi T. I., 2014, *The Astrophysical Journal*, 782, 81

This paper has been typeset from a \TeX / \LaTeX file prepared by the author.